Heliyon

ELSEVIER

Received:
12 August 2018
Revised:
5 November 2018
Accepted:
4 December 2018

Cite as: Elia Marin, Satoshi Horiguchi, Matteo Zanocco, Francesco Boschetto, Alfredo Rondinella, Wenliang Zhu, Ryan M. Bock, Bryan J. McEntire, Tetsuya Adachi, B. Sonny Bal, Giuseppe Pezzotti. Bioglass functionalization of laser-patterned bioceramic surfaces and their enhanced bioactivity.
Heliyon 4 (2018) e01016.
doi: 10.1016/j.heliyon.2018.e01016

Bioglass functionalization of laser-patterned bioceramic surfaces and their enhanced bioactivity

Elia Marin [a,b,*], **Satoshi Horiguchi** [b], **Matteo Zanocco** [a], **Francesco Boschetto** [a], **Alfredo Rondinella** [a], **Wenliang Zhu** [a], **Ryan M. Bock** [c], **Bryan J. McEntire** [c], **Tetsuya Adachi** [b], **B. Sonny Bal** [c,d], **Giuseppe Pezzotti** [a,f,g,e]

[a] *Ceramic Physics Laboratory, Kyoto Institute of Technology, Sakyo-ku, Matsugasaki, 606-8585 Kyoto, Japan*

[b] *Department of Dental Medicine, Graduate School of Medical Science, Kyoto Prefectural University of Medicine, Kamigyo-ku, Kyoto 602-8566, Japan*

[c] *Amedica Corporation, 1885 West 2100 South, Salt Lake City, UT, USA*

[d] *Department of Orthopaedic Surgery, University of Missouri, Columbia, MO, USA*

[e] *Department of Immunology, Graduate School of Medical Science, Kyoto Prefectural University of Medicine, Kamigyo-ku, 465 Kajii-cho, Kawaramachi dori, 602-0841 Kyoto, Japan*

[f] *Department of Orthopedic Surgery, Tokyo Medical University, 6-7-1 Nishi-Shinjuku, Shinjuku-ku, 160-0023 Tokyo, Japan*

[g] *The Center for Advanced Medical Engineering and Informatics, Osaka University, Yamadaoka, Suita, 565-0871 Osaka, Japan*

* Corresponding author at: Ceramic Physics Laboratory, Kyoto Institute of Technology, Sakyo-ku, Matsugasaki, 606-8585 Kyoto, Japan.
E-mail address: elia-marin@kit.ac.jp (E. Marin).

Abstract

The surfaces of silicon nitride (β-Si_3N_4) and zirconia toughened alumina (ZTA) were patterned using a high-energy laser source, which operated at a wavelength of 1064 nm. The patterning procedure yielded a series regular, cylindrical cavities 500 and 300 μm in diameter and depth, respectively. These cavities were subsequently filled with bioglass mixed with different fractions of Si_3N_4 powder (0, 5, and 10 mol.%) to obtain bioactive functionalized bioceramic surfaces. The laser-patterned samples were first characterized using several spectroscopic techniques before and after functionalization, and then tested in vitro with respect to their

https://doi.org/10.1016/j.heliyon.2018.e01016

osteoconductivity using a human osteosarcoma cell line (SaOS-2). After in vitro testing, fluorescence microscopy was used to address the biological response and to estimate osteopontin and osteocalcin protein contents and distributions. The presence of bioglass greatly enhanced the biological response of both ceramic surfaces, but mainly induced production of inorganic apatite. On the other hand, the addition of minor fraction of Si_3N_4 into the bioglass-filled holes greatly enhanced bio-mineralization and stimulated the SaOS-2 cells to produce higher amounts of bone extracellular matrix (collagen and proteins), thus enhancing the osteopontin to osteocalcin ratio. It was also observed that the presence of a fraction of Si_3N_4 in the powder mixture filling the holes bestowed more uniform cell colonization on the otherwise bioinert ZTA surface.

Keywords: Biomedical engineering, Materials chemistry, Materials science

1. Introduction

Bioceramics have increasingly been employed to replace metallic components with the purpose of exploiting their friendly behaviour in the human body. The most common bioceramics on the market are nowadays oxides including alumina (Al_2O_3), zirconia (ZrO_2) and zirconia-toughened alumina (ZTA) [1, 2]. Believed to possess intrinsic chemical stability, oxide bioceramics have long been considered to be completely bioinert, meaning that they induce no measurable reactions with biological tissues. Note, however, that this definition refers to "standard working conditions", thus excluding complications, such as the formation of wear debris. Moreover, no specific "response limit" has yet been provided [3]. Exploiting an improved chemical stability in the human body certainly represents a great improvement in comparison with metals, whose overestimated bioinertness has brought on a number of unfortunate consequences in patients, including hypersensitivity [4] and pseudo-tumour formation caused by wear debris [5] (e.g., reported as two of the major causes for revision surgery in orthopaedic implants [6]). Such adverse effects can be greatly mitigated by employing oxide bioceramics, although they are not completely eliminated [7]. There are indeed few studies that report adverse reactions to ceramic oxide debris. High levels of tumour necrosis factor (TNF) were revealed by in vitro testing Al_2O_3 debris vs. human peripheral blood mononuclear cells [8]. In addition, both Al_2O_3 and ZrO_2 debris were found to induce tissue inflammation during *in vivo* testing in a murine model [9]. Therefore, the search for new bioceramics with friendly chemistry and improved biological response in the human body is yet ongoing.

Recently, the non-oxide bioceramic silicon nitride (Si_3N_4), has emerged as a suitable material for spinal implant applications [10]. This material offers a mechanical performance comparable if not even superior in toughness to bioceramic oxides.

Moreover, both retrieval analysis and in vitro experiments have shown that this non-oxide ceramic can enhance differentiation of mesenchymal progenitor cells into osteoblasts [11], and promote osteoblastic activity [12]. Similarly to bioglasses [13] and hydroxyapatite/calcium phosphate based materials [14], Si_3N_4 greatly promotes the formation of bone tissue. This arises from the presence of both negatively and positively charged terminal groups on its surface, which promotes cell adhesion, and to its pH-dependent ability to concurrently release ammonia and silicic acid into the surroundings [15]. The chemical stimulus for bone tissue formation by both mesenchymal and osteoblast cells were related to NO elution, which is interpreted by the cells as a signal for proliferation and activity [11, 12].

Lasers represent invaluable tools in modern materials processing. They can be used to alter the surface stoichiometry of a biomaterial, to texture it at different length scales, to engineer the surface of biomedical components with generating complex patterns, and even to produce new materials. By exploiting modern laser technologies, it is possible to create advanced biomedical devices that exhibit unique biological characteristics and patient-specific attributes at their surface. Laser processing of biomaterials also presents several advantages over other methods, namely low surface contamination, low mechanical damage, and high output controllability in processing geometrically complex three-dimensional components [16]. These advantages combined with the multiple choices offered by lasers with different wavelengths have recently stimulated a number of research efforts, which include surface modifications with textures, patterns, and coatings [17, 18, 19], and the fabrication of complex three-dimensional parts from bulk blocks of biomaterials [20].

In this study, Si_3N_4 and ZTA bulk bioceramics were laser-patterned on their surfaces at the scale of the hundreds of micrometers. The cavities obtained by such patterning were filled with powder mixtures of bioglass and Si_3N_4 in different fractions with the scope of functionalizing the surfaces for an increased bioactivity. In this study, we monitored cell proliferation, bone tissue formation, and quality of bone tissue in terms of mineral-to-matrix ratio. This attempt represents a first step toward a multiscale surface engineering aimed at tailoring the surface of bioceramics for different applications in the human body such as improved osteointegration of ceramic spinal implants.

2. Experimental

2.1. Substrate samples

Sintered β-Si_3N_4 discs were provided by Amedica Corporation (Salt Lake City, UT). The disc samples had diameter and thickness of 12.7 mm and 3 mm, respectively. The

 https://doi.org/10.1016/j.heliyon.2018.e01016

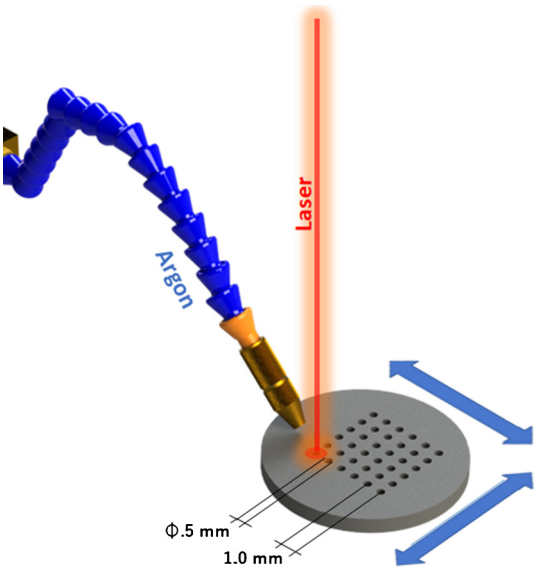

Figure 1. Schematic draft of the procedure of surface patterning by laser beam.

Si_3N_4 material consisted of a two-phase microstructure including acicular β-Si_3N_4 grains separated by a continuous and sub-micrometric sized film of Si–Y–Al–O–N grain-boundary phase. ZTA samples (Biolox® delta, CeramTec, GmbH, Plochingen, Germany) were machined starting from 36 mm diameter femoral heads (year of production: 2014) [21] in squared slabs of 1 × 1 cm with a thickness of 3 mm using a slow speed diamond coated blade. All used surfaces were finely polished down to the scale of the tens of the nanometer. Polished titanium Grade 5 alloy (Ti–6Al–4V ELI) discs were used for comparison.

2.2. Laser patterning

Laser patterning was performed using a Vision LWI V ERGO-Workstation mounting a Nd:YAG laser with a wavelength of 1064 nm. The focusing distance was 25 cm, the nominal maximum power was 17 kW, and the burst energy was up to 70 J. The applied potential and discharge time were regulated in the range 160∼500 V and 1∼20 ms, respectively. The work-station was equipped with a gas nozzle connected to an Argon source at 1.2 Atm to prevent oxidation. A motorized x–y stage with a precision of 10 μm was used to align the sample with the laser source and to produce a regular grid of equidistant cavities with an interspace of 1.0 mm. A schematic drawing of the sample production protocol is presented in Figure 1.

2.3. Bioglass preparation

Standard 45S5 Bioglass® powder (Mo-Sci Corporation, Rolla, MO, USA) was preliminary mixed with 5 or 10 mol.% α-Si_3N_4 powder with nanometer scale particle

https://doi.org/10.1016/j.heliyon.2018.e01016

Table 1. Composition of the bioglass used in the present experiments.

Bioglass	SiO_2 %	CaO %	Na_2O %	P_2O_5 %	Si_3N_4 %
Standard	45.00	24.50	24.50	6.00	–
5% Si_3N_4	41.22	23.72	23.72	5.83	5.51
10% Si_3N_4	37.66	23.00	23.00	5.65	10.69

size. The α-Si_3N_4 powder was a commercially available brand (SN-E10, Ube Co., Ube City, Japan). Powder mixtures of bioglass with 5 and 10 mol.% α-Si_3N_4 had compositions in wt.% as shown in Table 1 (measured by the authors on batches prepared by Mo-Sci Corporation). After mixing and homogenizing the powders, each patch was melted in a platinum crucible in N_2 atmosphere, and subsequently quenched, crushed, and commuted back into fine powder.

2.4. Cell culture studies

The SaOS-2 human osteosarcoma cell line was selected for its capacity of quickly producing bone tissue. The cells were first cultured and incubated in an osteoblast-inducer medium consisting of 4.5 g/l of glucose DMEM (D-glucose, L-glutamine, phenol red, and sodium pyruvate) and containing 10% of fetal bovine serum. Cells were allowed to proliferate within Petri dishes for 24 h at 37 °C. The final SaOS-2 concentration was equal to 5×10^5 cell/mL. The cultured cells were then deposited on the top surface of previously UV-sterilized samples and unpatterned controls. Cell seeding was performed using an osteogenic medium consisting of DMEM supplemented with 50 μg/mL of ascorbic acid, 10 mM β-glycerol phosphate, 100 mM hydro-cortisone, and 10% fetal bovine calf serum. All samples were concurrently tested for their osteoconductivity upon incubation of 168 h at 37 °C.

2.5. Sample characterization

2.5.1. Fluorescence microscope

After exposure to osteoblasts, each batch of different samples was observed using fluorescence microscopy (BZ-X700; Keyence, Osaka, Japan). Prior to examination, the samples surfaces were treated with different immunostaining reagents, including Hoechst 33342 (Dojindo, Kumamoto, Japan), anti-Human Osteocalcin Clone 2H9F11F8, Isotype IgG, Rabbit polyclonal antibody (IBL, Gunma, Japan). Hoechst 33342, a cell nucleus stain, served to visualize cell proliferation, while the other two antibodies were used to stain matrix proteins osteocalcin and osteopontin, respectively, whose concentration quantifies the process of mineralization and bone

matrix formation. Subsequently, a secondary antibody, Goat anti-Mouse IgG1 Antibody FITC Conjugated (Bethly Laboratories) was added to enhance signal detection and visualization.

2.5.2. Laser microscope

Micrographs were taken by mean of a 3D laser-scanning microscope (VKX200K series, Keyence, Osaka, Japan) with magnifications ranging from 10× to 150× with numerical apertures between 0.30 and 0.95. The microscope was equipped with an automated x–y stage and with autofocus function for the z-range. Assembled maps covering the entire surface of the tested samples were then used for calculating both areas and volumes of the bone tissue grown by SaOS-2 cells on the respective sample surfaces.

2.5.3. FTIR spectroscopy

FTIR spectra were obtained using a high sensitivity spectroscope (Spectrum 100FT-IR Spotlight400; Perkin-Elmer Inc., Waltham, MA, USA). The spectral resolution of this equipment was 0.4 cm^{-1}. Average FTIR spectra were computed for each substrate from eight independent measurements. Pre-processing of raw data included baseline subtraction, smoothing, normalization, and fitting of the raw spectra using "R" [22].

2.6. Statistical significance

To ensure statistical significance, all biological testing was performed n = 6 times. Three randomly selected samples for each batch were used for fluorescence microscopy, while the remaining three were used for FTIR and laser microscopy.

3. Results

3.1. Preliminary characterization

3.1.1. Laser drilling calibration

The depth and diameter of the cylindrical holes obtained by laser drilling were accurately calibrated upon controlling four parameters: laser focusing diameter (f), applied voltage (V), discharge time (t), and number of bursts (n). Figures 2 and 3 show the results obtained on Si_3N_4 by optical microscopy and laser topography,

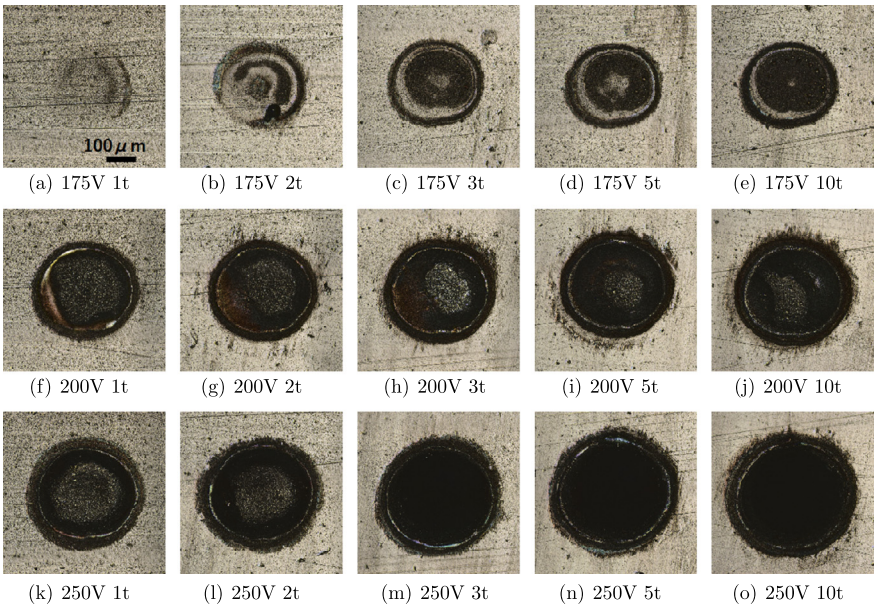

Figure 2. Optical micrographs showing the results of a calibration procedure on laser power to achieve cylindrical holes 500 and 300 μm in diameter and depth, respectively.

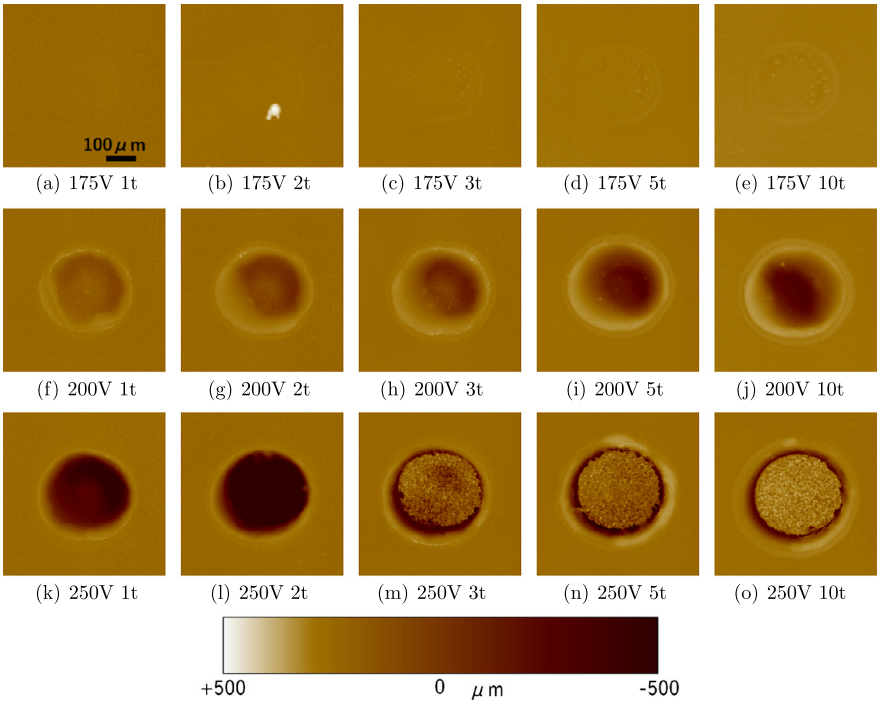

Figure 3. Laser topographical micrographs showing the results of a calibration procedure on laser power to achieve a cylindrical hole 500 and 300 μm in diameter and depth, respectively.

respectively. The figures refer to a discharge time of 4 ms and a focusing diameter of 500 μm.

https://doi.org/10.1016/j.heliyon.2018.e01016

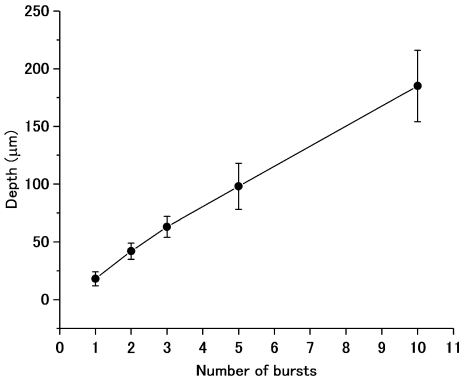

Figure 4. Dependence of cylindrical hole depth upon number of laser bursts (applied voltage 200 V, focusing area = 500 μm).

During preliminary calibrations, the focusing diameter was increased from 250 to 1500 μm at steps of 50 μm. However, an optimal diameter for the cylindrical holes was selected according to literature concerning osseointegration of porous implants, coatings, and scaffolds [23]. Scientific studies on this topic suggested different ranges for the porosity size. Although these suggestions strongly depended on type of material, pore shape, wall roughness and size distribution [24, 25, 26], there was general consensus in indicating porosities in the range 100∼500 μm diameter for optimal adhesion, proliferation, and stimulation of osteoblastic activity.

It was observed that, even at relatively low applied voltages (200 V, Figures 3(f) and 2(f)), the energy density of the beam sufficed to reach the sublimation temperature of Si_3N_4 (∼1900 °C [27]), thus producing a cavity with sharp borders. In comparison, an applied voltage of about 175 V (Figures 2(a) and 3(a)) could not produce any significant morphological alteration of the surface. Increasing the number of laser bursts at the applied potential of 175 V led to the formation of dark, oxidized spots without damaging the material underneath (Figures 3(a–e) and 2(a–e)). For an applied potential of 200 V and a spot size of 500 μm (Figures 3(f–j) and 2(f–j)), the depth of the holes grew almost linearly with the number of laser bursts, as shown in Figure 4. For higher applied potentials (Figures 3(k–o) and 2(k–o)), additional phenomena were observed: (i) a porous, (likely N-defective) Si_3N_4 sponge was produced at the bottom of the cavity; and, (ii) by exceeding 250 V, solidified droplets were re-deposited in the surrounding areas often partially occluding the porosities (not shown). Taking into consideration these observations, two bursts of 4 ms at an applied potential of 250 V were selected as the optimal range for the fabrication of regular homogeneous holes 500 and 300 μm in diameter and depth, respectively. The same laser parameters were also applied to the ZTA substrate resulting in overall comparable hole geometry. However, unlike Si_3N_4, which tends to vaporize under the laser beam, ZTA melted and was ejected from the pool upon laser beam impingement. While this different behaviour in the oxide ceramic did not affect the

 https://doi.org/10.1016/j.heliyon.2018.e01016

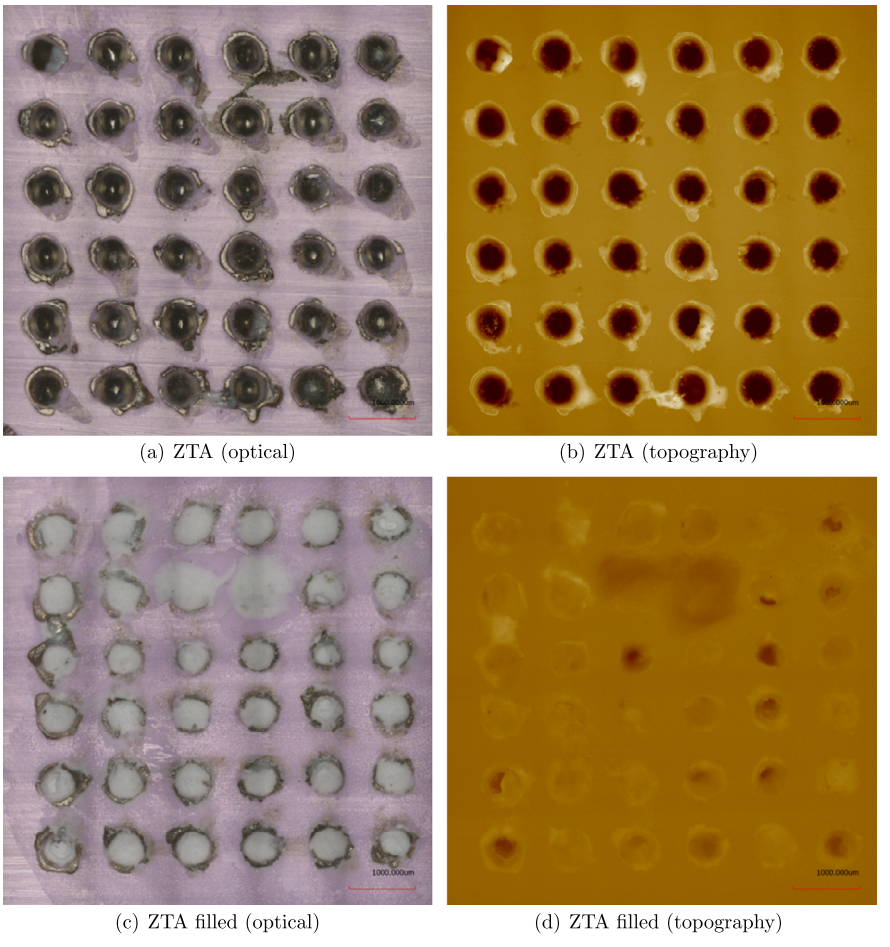

(a) ZTA (optical) (b) ZTA (topography)

(c) ZTA filled (optical) (d) ZTA filled (topography)

Figure 5. Optical and laser topographical micrographs of a 6 × 6 laser texture on the investigated ZTA surface before (a, b) and after (c, d) hole-filling with bioglass.

geometry of the drilled holes, additional care was required during operation in order to avoid burns by the ejected matter.

Figures 5(a–b) and 6(a–b) show 6 × 6 grids of cylindrical holes as obtained by applying the above-mentioned parameters in the case of ZTA and Si_3N_4 substrates, respectively. In comparing these two figures, it can be observed that, while the shape of the holes on the non-oxide sample is regular with clear and sharp edges, holes patterned on the ZTA substrate present splashes of melted material surrounding irregularly shaped channels with partly distorted edges. This was a clear indicator of the different behaviour in laser drilling of oxide and non-oxide bioceramics.

General consensus indicates that, for holes in the range 100–500 μm diameter, adhesion, proliferation and stimulation of osteoblastic activity leads to faster and healthier bone tissue ingrowth.

 https://doi.org/10.1016/j.heliyon.2018.e01016

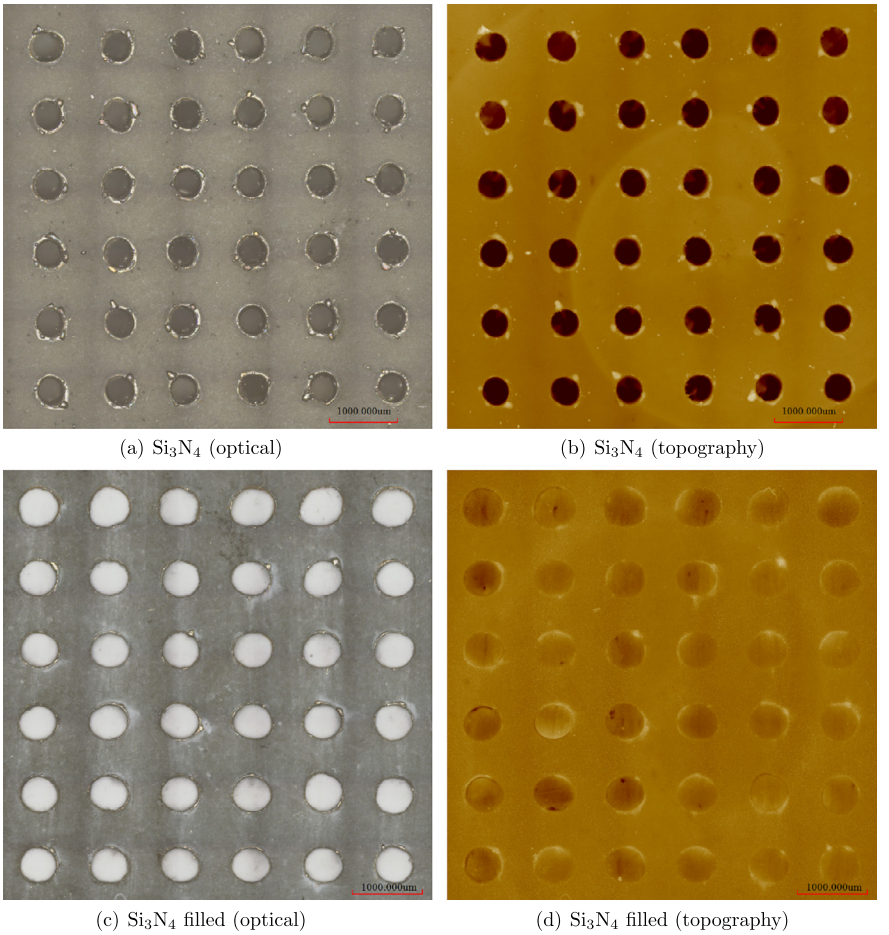

(a) Si_3N_4 (optical) (b) Si_3N_4 (topography)

(c) Si_3N_4 filled (optical) (d) Si_3N_4 filled (topography)

Figure 6. Optical and laser topographical micrographs of a 6 × 6 laser texture on Si_3N_4 surface before (a, b) and after (c, d) hole-filling with bioglass.

3.1.2. Bioglass filling

The procedure of filling the laser-patterned cylindrical holes consisted of first pressing the bioglass/Si_3N_4-powder mixtures into the surface using a laboratory spatula, and then manually removing the excess materials using a sharp blade. No additional effort was needed to keep the powders inside the holes; because of its relatively strong cohesion and adhesion to the walls for hole diameters ~500 μm. The results of optical and laser microscopy observations, which document the bioglass filling procedure for ZTA and Si_3N_4, are shown in Figures 5(c–d) and 6(c–d), respectively. In both cases, it was observed that the holes were completely filled with bioglass.

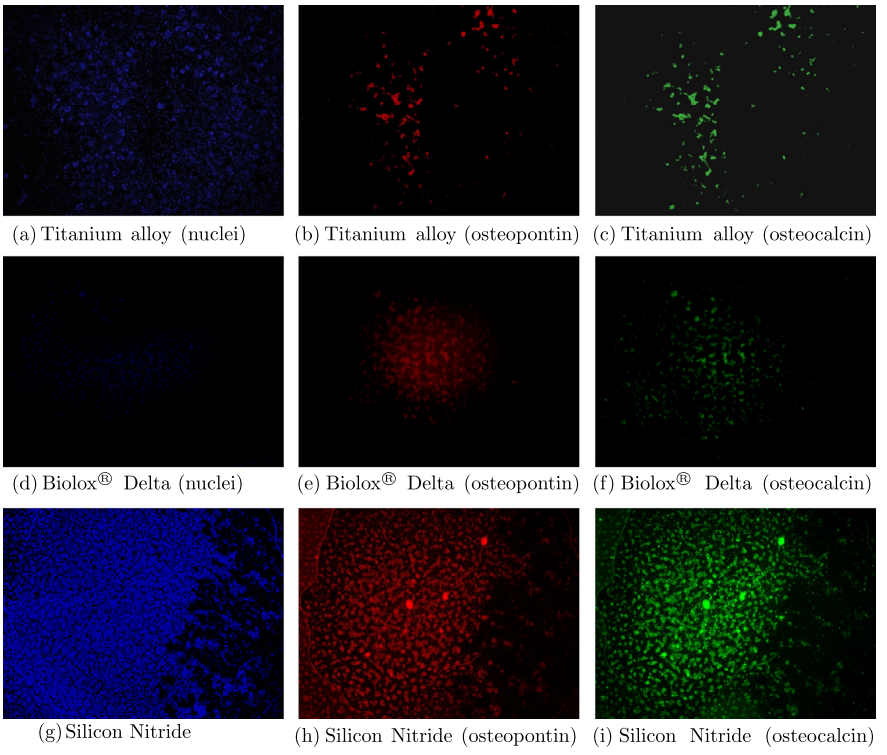

Figure 7. Fluorescence microscopy images collected on titanium alloy control (a~c), ZTA (d~f), and Si_3N_4 (g~i) pristine substrates: blue stain (osteoblast nuclei), red stain (osteopontin), and green stain (osteocalcin).

3.2. In vitro osteoconductivity

3.2.1. Fluorescence microscope

Figure 7 shows the results of fluorescence microscopy obtained on unpatterned ZTA and Si_3N_4 substrates after exposure to SaOS-2 cells for 168 h. A biomedical titanium alloy substrate was also tested for comparison. Both titanium alloy and Si_3N_4 promoted cell proliferation on their surface (Figure 7a and g, respectively), which in turn resulted in an enhanced formation of mineralized tissue (Figure 7b, c and h, i) as seen from tagging both osteopontin and osteocalcin. However, while mineralized tissue concentrated at separate spots on the titanium alloy substrate, it appeared quite uniformly distributed overall the entire Si_3N_4 surface. As for the pristine ZTA substrate, (Figure 7d, e, f), no cell proliferation and only quite weak signals of osteocalcin/osteopontin were found, which indicates a very limited, if any, bioactive response of this substrate to osteoblasts.

Figure 8 summarizes the results of SaOS-2 experiments on hole-patterned Si_3N_4 substrates with and without filling with 0, 5, and 10 mol.% Si_3N_4-containing bioglass powders. Cell proliferation and production of osteopontin and osteocalcin were

 https://doi.org/10.1016/j.heliyon.2018.e01016

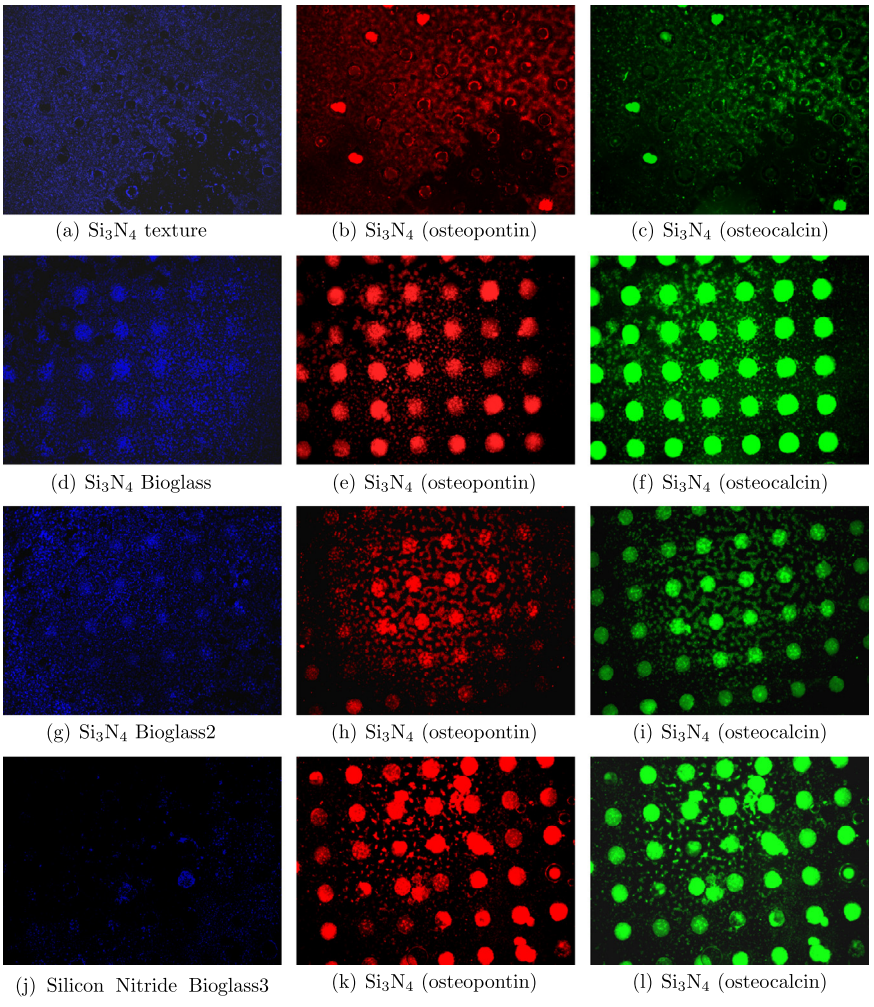

Figure 8. FM images collected on Si_3N_4 patterned and unfilled surface (a~c), Si_3N_4 patterned and filled with bioglass only (d~f), Si_3N_4 patterned and filled with bioglass-5 mol.% Si_3N_4 mixture (g~i), and Si_3N_4 patterned and filled with bioglass-10 mol.% Si_3N_4 mixture (j~l): blue stain (osteoblast nuclei), red stain (osteopontin), and green stain (osteocalcin).

observed on all patterned Si_3N_4 substrates, but signals from both osteocalcin and osteopontin strongly increased in substrates with filled patterns. It is important to note that the presence of osteopontin in mineralized tissue grown on Si_3N_4 is important because it shows that this material stimulates the production of biological matrix together with mineralized apatite.

Figure 9 shows the results of experiments similar to those described in Figure 8, as obtained on patterned ZTA samples after the SaOS-2 tests. Unfortunately, emissions from osteopontin staining (Figure 9b, e, h, k) overlapped with the intrinsic red fluorescence of the substrate (i.e., due to Cr-dopant, present in the ZTA material). This phenomenon greatly disturbed the detection of osteopontin. However, neither osteopontin nor osteocalcin, whose green emissions were undisturbed by the

 https://doi.org/10.1016/j.heliyon.2018.e01016

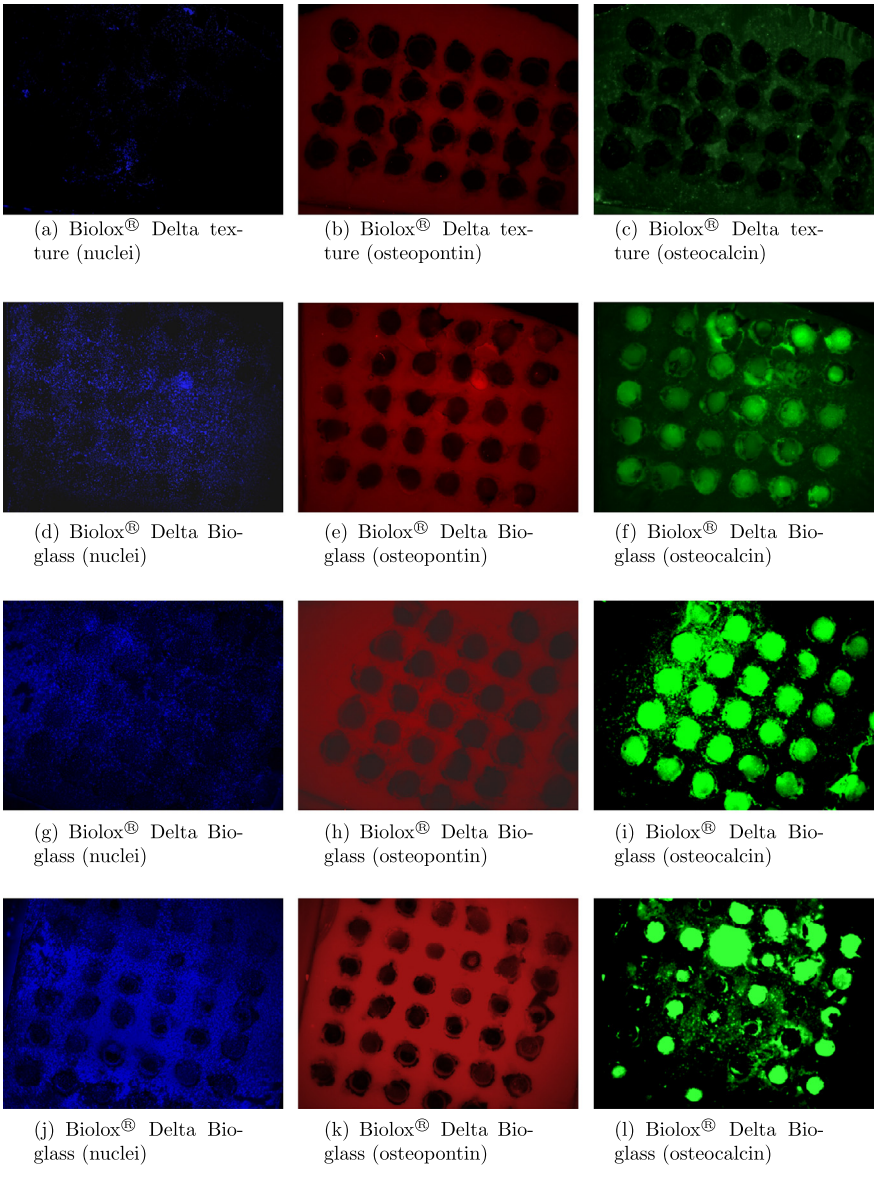

(a) Biolox® Delta texture (nuclei)
(b) Biolox® Delta texture (osteopontin)
(c) Biolox® Delta texture (osteocalcin)
(d) Biolox® Delta Bioglass (nuclei)
(e) Biolox® Delta Bioglass (osteopontin)
(f) Biolox® Delta Bioglass (osteocalcin)
(g) Biolox® Delta Bioglass (nuclei)
(h) Biolox® Delta Bioglass (osteopontin)
(i) Biolox® Delta Bioglass (osteocalcin)
(j) Biolox® Delta Bioglass (nuclei)
(k) Biolox® Delta Bioglass (osteopontin)
(l) Biolox® Delta Bioglass (osteocalcin)

Figure 9. FM images collected on ZTA patterned and unfilled surface (a~c), ZTA patterned and filled with bioglass only (d~f), ZTA patterned and filled with bioglass-5 mol.% Si_3N_4 mixture (g~i), and ZTA patterned and filled with bioglass-10 mol.% Si_3N_4 mixture (j~l): blue stain (osteoblast nuclei), red stain (osteopontin), and green stain (osteocalcin).

intrinsic red fluorescence of the ZTA substrate, appeared in the ZTA surface with unfilled holes (Figures 9(b, c)). On the other hand, we observed an increase in cell proliferation on the ZTA surfaces by increasing the fraction of Si_3N_4 added to the bioglass filler (cf. blue emission from cell nuclei in Figures 9(a, d, g, j)). Moreover, the green osteocalcin fluorescence, which represented mineralized tissue regions, not only showed a strong signal from filled holes on all samples, but it also expanded

https://doi.org/10.1016/j.heliyon.2018.e01016

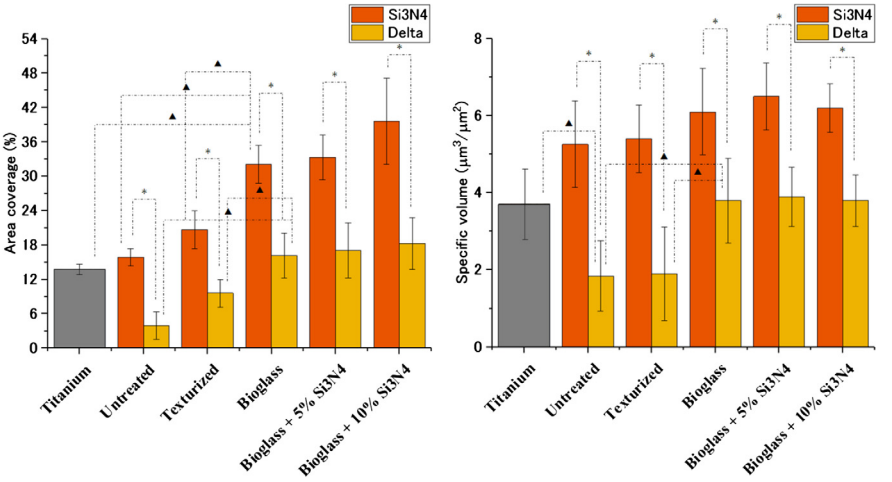

(a) Biological tissue area coverage (b) Biological tissue specific volume

Figure 10. Summary of quantitative laser microscopy analyses on *in vitro* biological tissue formation: (a) biological tissue area coverage and (b) volume of biological tissue per unit of area, as measured on different samples. Areas coinciding with the bioglass filled porosities have been excluded from the calculations. Triangles and asterisks indicate a p value ≤0.01 among different treatments and substrates, respectively.

into unpatterned regions of the sample surface when the bioglass hole filler contained 10 mol.% Si_3N_4 (Figure 9(l)).

3.2.2. Laser microscopy

Figure 10 summarizes the full set of quantitative data acquired by laser microscopy. The plot in (a) shows biological tissue area coverage for different substrates, while the plot in (b) gives the specific volume of the grown biological tissue per square micron of surface. In both data sets, holes (and related fillers) were excluded from the calculation in an attempt to limit the level of inaccuracy. The bone-tissue area coverage on untreated Si_3N_4 was about 500% higher than that of ZTA and 15% higher than that of the titanium alloy control (Figure 10(a)). These data confirm the biologically friendly nature of Si_3N_4, whose peculiar surface chemistry stimulates cell proliferation and biological tissue production. The presence of a regular grid of cylindrical holes filled with bioglass/Si_3N_4 mixtures increased the fraction of apatite-covered areas in both oxide and non-oxide substrates. In particular, the coverage on the ZTA substrate was almost doubled. Clearly, the addition of bioglass filler stimulated the biological response, but such an improvement appeared to be further boosted when a fraction of Si_3N_4 was added to the bioglass mixture. Similar trends were observed for specific biological tissue volume gain per unit area (Figure 10(b)), although with a larger statistical scatter caused by the uncertain morphology of the pristine substrates. When compared to areal fractions, the volume

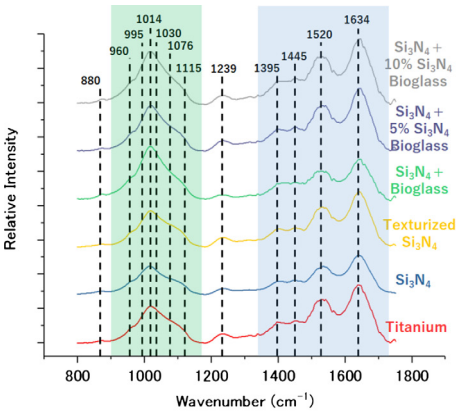

(a) FTIR (Silicon Nitride)

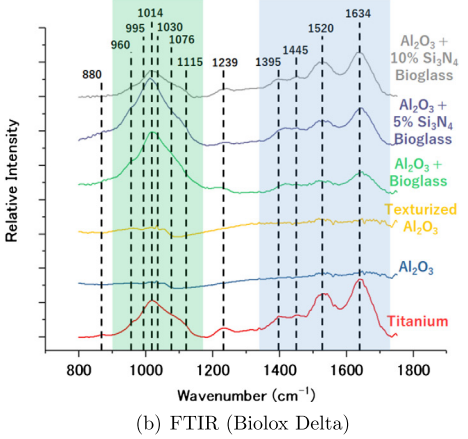

(b) FTIR (Biolox Delta)

Figure 11. FTIR spectra collected on (a) Si_3N_4 and (b) ZTA substrates before and after patterning/filling of the hole grid. The signal intensities in the two spectral regions marked in green (at 900~1000 cm^{-1}) and blue (at 1340~1700 cm^{-1}) light colours represent the mineral apatite crystal and the organic collagen fractions, respectively. The integrated areal ratio of these two spectral zones has been used to estimate the composition of the mineralized tissue produced by SaOS-2 cells.

of biological tissue grown on Si_3N_4 appears to be less affected by the presence of the filler, while such presence was crucial in obtaining a bioactive ZTA substrate.

3.2.3. FTIR spectroscopy

Figures 11(a) and (b) show FTIR spectra acquired on Si_3N_4 and ZTA substrates, respectively, in comparison with the titanium alloy substrate control. All bands in the spectra are described with respect to their spectral locations and physical origins in Table 2.

Two main points were extracted from the spectra, which were common to both figures: (i) The addition of only bioglass filler led to an increase in signal intensity in the spectral area around 1000 cm^{-1}, which is associated with hydroxyapatite; and,

 https://doi.org/10.1016/j.heliyon.2018.e01016

Table 2. Band positions and physical origin of the bands recorded in the FTIR spectrum of SaOS-2 grown mineralized tissue.

Band	Position	Assignment	Reference
1	880 cm^{-1}	CO_3^{2-}	[28]
2	960 cm^{-1}	PO_4^{3-} (v_1)	[28]
3	995 cm^{-1}	PO_4^{3-} (v_1)	[28]
4	1014 cm^{-1}	PO_4^{3-} (v_1)	[28]
5	1030 cm^{-1}	PO_4^{3-} (v_3)	[28]
6	1076 cm^{-1}	PO_4^{3-} (v_3)	[28]
6	1114 cm^{-1}	PO_4^{3-} (amorphous apatite)	[28]
7	1239 cm^{-1}	Amide III	[28]
8	1395 cm^{-1}	CH_2	[29]
9	1445 cm^{-1}	CH_2 bend, PO_4^{3-}	[29]
10	1520 cm^{-1}	Amide II	[29]
11	1634 cm^{-1}	Amide I	[29]

(ii) The addition of a fraction of Si_3N_4 to the bioglass filler led to an increase in relative intensity for bands at around 1500 cm^{-1}, which are associated with amides and represent the biological matrix of the mineralized tissue.

Both (i) and (ii) were observed to some extent also for Si_3N_4 substrates (Figure 11(a)). Specifically, the addition of only bioglass as filler in patterned Si_3N_4 led to a relatively stronger signal of the mineral fraction at around 1000 cm^{-1} with respect to the signal of biological matrix at around 1500 cm^{-1}. On the other hand, no mineralized tissue was detected on either pristine or patterned ZTA substrates in the absence of filler (Figure 11(b)). However, the presence of filler greatly enhanced both mineral signals in ZTA, while the presence of minor fractions of Si_3N_4 in the bioglass filler induced an increase in the relative intensity of the biological matrix band.

Figure 12 summarizes this latter aspect with a plot of intensity ratios between apatite and organic matrix signals in the FTIR spectra as a function of the type of substrate. SaOS-2 cells on Si_3N_4 substrates produced mineralized tissue with inorganic/organic FTIR intensity ratios ~0.5, which were comparable to that of the mineralized tissue grown on biomedical grade titanium alloy. Addition of only bioglass as a filler in the patterned holes caused an increase in the intensity of hydroxyapatite-related bands, especially significant in ZTA. The balance between inorganic and organic constituents was compensated by adding minor fractions of Si_3N_4 into the bioglass mixture. On pristine ZTA substrates, no signal from mineralized tissue was resolved, but the addition of bioglass increased the relative intensity of the hydroxyapatite/collagen signal ratio up to ~2.5 times above those recorded for the pristine Si_3N_4 substrate. Addition of 10% fraction of Si_3N_4 in the filler was required to bring the inorganic/organic band ratio of ZTA in the same range as titanium alloy.

Results presented in Figure 12, show the area intensity ratio of the two regions marked on Figures 11(a) and (b) plotted as a function of substrate. Si_3N_4 was able to

produce mineralized tissue with similar mineral over amide ratios when compared to biomedical grade titanium alloys. Additions of standard Bioglass caused an increase in the intensity of the phosphate-related bands, which was compensated by adding relatively small amounts of Si_3N_4 into the Bioglass mixture. For Biolox® delta, the signal intensity was too low to be properly resolved, but the addition of standard Bioglass increased the relative intensity of phosphate-related bands about 2.5 times more than for Si_3N_4 substrates. Adding Si_3N_4 to the Bioglass mixture again reduced the relative intensity of phosphate-related bands, but only about 10% of Si_3N_4 was required in order to obtain values in the same range as titanium alloy. Following previous literature results obtained on the same bioglasses using Raman Spectroscopy after osteosarcoma treatment [30], and in particular the relative intensity and position of the band at about 960 cm^{-1}, it can be assumed that the phosphate structures observed by FTIR are organized into hydroxyapatite crystals.

3.2.4. Laser microscopy

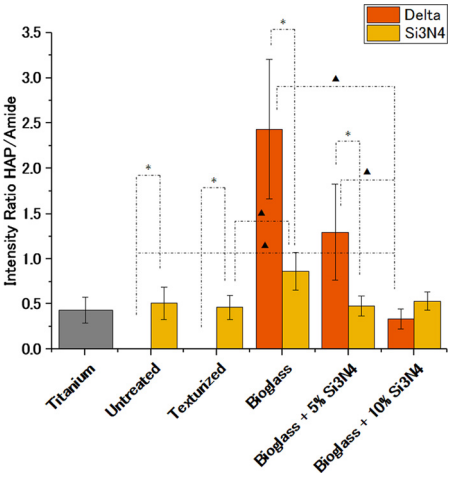

Figure 12. Integrated areal ratio of mineral apatite on organic collagen signals as measured by FTIR spectroscopy on different samples.

4. Discussion

The key results of this study are schematically summarized in Figure 13, with the ratio of inorganic (hydroxyapatite; H) to organic (amide; A) tissue components, as quantified by FTIR, indicated on the flank of each item. Osteoblasts are drawn in blue, while red and green spots represent osteopontin and osteocalcin (as visualized by fluorescence microscopy). The coloured arrows on the top left give a qualitative estimate of the surface pH based on literature references, from about 7 (green) to about 9 (dark blue) [31, 32, 33]. The schematic also shows the control sample made

 https://doi.org/10.1016/j.heliyon.2018.e01016

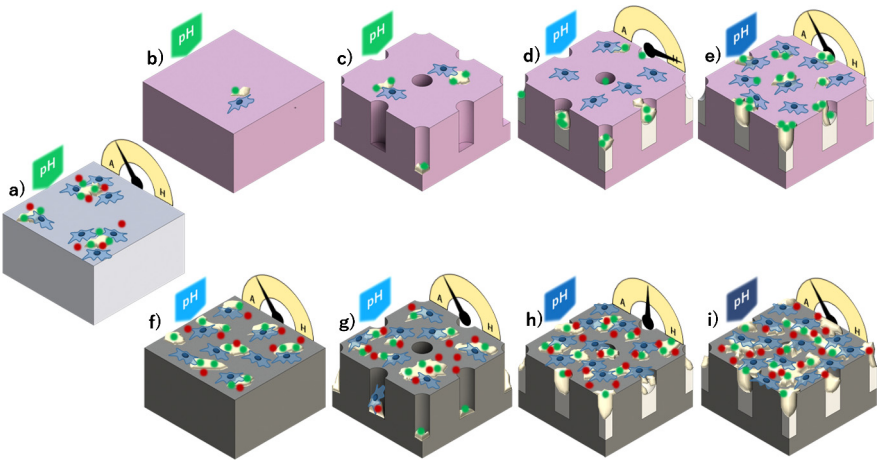

Figure 13. Schematic draft summarizing the main research findings from in vitro osteoconductivity experiments conducted on different substrates before and after patterning/texturing: amounts of mineralized tissue, osteocalcin, osteopontin, cell colonization, and FTIR intensity ratio between mineral apatite crystal (H) and the organic collagen (A) are represented as a function of surface pH; biomedical titanium alloy (a), unpatterned and patterned ZTA (b~e), and unpatterned and patterned Si_3N_4 (f~i).

of biomedical titanium alloy (Figure 13(a)), which was bioactive but, ultimately, only capable of stimulating a localized production of large clusters of mineralized tissue rather than a full coverage. The two investigated ceramic substrates showed opposite behaviours. Unpatterned ZTA (Figure 13(b)) conspicuously failed in stimulating the production of mineralized tissue, while the unpatterned surface of Si_3N_4 (Figure 13(f)) was completely colonized by the SaOS-2 cells and fully covered by mineralized tissue with a hydroxyapatite/amide (H/A) ratio comparable to titanium alloy. Patterning alone (Figures 13(c) and (g)) did not significantly improve the bioactivity of either substrate. However, filling the patterns with bioglass (Figures 13(d) and (h)) stimulated SaOS-2 cells to produce higher amounts of mineralized hydroxyapatite on both types of ceramic substrates, resulting in an extremely high H/A ratio for the patterned/filled ZTA. Adding Si_3N_4 to the bioglass filler (Figures 13(e) and (i)) always resulted in mineralized tissue with a higher amount of osteopontin.

The osseoconductive properties of Si_3N_4 have been thoroughly explored in literature [34, 35]. It was reported that the presence of both positive and negative charges resulted in a great improvement in viability, proliferation, and differentiation into osteoblasts [36, 37]. In addition, it has been shown that the presence of Si_3N_4 can effectively increase the pH of the surrounding environment [32], thus promoting both calcium phosphate precipitation [38] and extracellular matrix formation. On the other hand, bioglass acts as a source of ions that osteoblasts can use to produce hydroxyapatite [39], while also promoting the spontaneous formation of calcium phosphate crystals [40] that are incorporated into the newly formed mineralized tissue. This process of spontaneous mineralization leads to the generation of highly

 https://doi.org/10.1016/j.heliyon.2018.e01016

mineralized tissue with a relatively low amount of extracellular matrix [41]. As schematically depicted in Figures 13(b) and (c), bioglass by itself does not promote surface colonization. As a matter of fact, cell nuclei were observed colonizing on ZTA only when the bioglass filler was added with Si_3N_4.

Even if the osseoconductive properties of both ceramics resulted to be greatly improved by surface texturing and bioglass introduction, doubts may still rise about the influence of texturing on the mechanical properties. Surface texturing has been proved to be a viable tool for the improvement of wear and fretting resistance of a wide range of materials [42], but porosities can still act as a crack triggering location during static and dynamic mechanical loading [43]. The pore geometry, size and interaxes have been selected trying to minimize the risk of crack triggering or structural collapse [44, 45].

5. Conclusions

We investigated the response of SaOS-2 cells to different ceramic surfaces patterned with cylindrical holes which were filled with bioglass and Si_3N_4-added modifications. Statistically significant differences were found between different substrates and between different compositions of the filler, which can be summarized as follows:

- Unlike Si_3N_4, ZTA possessed no bioactive properties *in vitro*;
- Surface patterning by itself did not appreciably influence the production of mineralized tissue on ZTA;
- Adding only bioglass as a filler in the pattern of cylindrical holes increased only the amount of mineralized hydroxyapatite on the ceramic substrates;
- The presence of Si_3N_4 in the filler, similar to the effect of the Si_3N_4 substrate itself, stimulated the production of higher amounts of biological matrix (seen as amide bands in the FTIR spectra);
- The addition of Si_3N_4 to the bioglass filler promoted cell colonization on the ZTA surface thus rendering this material bioactive.

In conclusion, laser patterning combined with bioglass/Si_3N_4 filling resulted in a viable tool to improve the bioactivity of structural ceramic im-plants. The release of ions from bioglass has long been known as a phenomenon leading to faster osteointegration of biomedical implants over time. However, we were able to demonstrate that adding a minor fraction of Si_3N_4 to bioglass led to larger cell colonization and to a more balanced composition of mineralized tissue even on bioceramic surfaces otherwise completely lacking bioactive properties.

 https://doi.org/10.1016/j.heliyon.2018.e01016

6. Data availability

The raw/processed data required to reproduce these findings cannot be shared at this time as the data also forms part of an ongoing study.

Declarations

Author contribution statement

Elia Marin: Conceived and designed the experiments; Wrote the paper.

Satoshi Horiguchi, Matteo Zanocco, Francesco Boschetto, Alfredo Rondinella: Performed the experiments.

Wenliang Zhu: Analyzed and interpreted the data.

Ryan M. Bock, Bryan J. McEntire, Tetsuya Adachi, B. Sonny Bal: Contributed reagents, materials, analysis tools or data.

Giuseppe Pezzotti: Conceived and designed the experiments.

Funding statement

This research did not receive any specific grant from funding agencies in the public, commercial, or not-for-profit sectors.

Competing interest statement

The authors declare the following conflict of interests: Ryan Bock, Bryan McEntire and Sonny Bal work for Amedica Corporation, Salt Lake City, UT, US.

Additional information

No additional information is available for this paper.

References

[1] I.C. Clarke, Role of ceramic implants. Design and clinical success with total hip prosthetic ceramic-to-ceramic bearings, Clin. Orthop. Relat. Res. (282) (1992) 19–30.

[2] J. Gallo, S. Barry Goodman, J. Lostak, M. Janout, et al., Advantages and disadvantages of ceramic on ceramic total hip arthroplasty: a review, Biomed. Pap. 156 (3) (2012) 204–212.

[3] M. Vallet-Regí, Ceramics for medical applications, J. Chem. Soc., Dalton Trans. (2) (2001) 97–108.

[4] J.L. Basko-Plluska, J.P. Thyssen, P.C. Schalock, Cutaneous and systemic hypersensitivity reactions to metallic implants, Dermatitis 22 (2) (2011) 65–79.

[5] D. Langton, S. Jameson, T. Joyce, N. Hallab, S. Natu, A. Nargol, Early failure of metal-on-metal bearings in hip resurfacing and large-diameter total hip replacement: a consequence of excess wear, Bone Joint J. 92 (1) (2010) 38–46.

[6] N. Hallab, K. Merritt, J.J. Jacobs, Metal sensitivity in patients with orthopaedic implants, J. Bone Jt. Surg. 83 (3) (2001) 428.

[7] N.J. Hallab, J.J. Jacobs, Biologic effects of implant debris, Bull. NYU Hosp. Joint Dis. 67 (2) (2009) 182.

[8] A. Hatton, J. Nevelos, J. Matthews, J. Fisher, E. Ingham, Effects of clinically relevant alumina ceramic wear particles on TNF-α production by human peripheral blood mononuclear phagocytes, Biomaterials 24 (7) (2003) 1193–1204.

[9] H. Warashina, S. Sakano, S. Kitamura, K.-I. Yamauchi, J. Yamaguchi, N. Ishiguro, Y. Hasegawa, Biological reaction to alumina, zirconia, titanium and polyethylene particles implanted onto murine calvaria, Biomaterials 24 (21) (2003) 3655–3661.

[10] R. Taylor, J. Bernero, A. Patel, D. Brodke, A. Khandkar, Silicon nitride: a new material for spinal implants, in: Orthopaedic Proceedings, vol. 92, The British Editorial Society of Bone & Joint Surgery, 2010, p. 133.

[11] G. Pezzotti, R.M. Bock, T. Adachi, A. Rondinella, F. Boschetto, W. Zhu, E. Marin, B. McEntire, B.S. Bal, O. Mazda, Silicon nitride surface chemistry: a potent regulator of mesenchymal progenitor cell activity in bone formation, Appl. Mater. Today 9 (2017) 82–95.

[12] G. Pezzotti, N. Oba, W. Zhu, E. Marin, A. Rondinella, F. Boschetto, B. McEntire, K. Yamamoto, B.S. Bal, Human osteoblasts grow transitional Si/N apatite in quickly osteointegrated Si_3N_4 cervical insert, Acta Biomater. 64 (2017) 411–420.

[13] G. Kaur, O.P. Pandey, K. Singh, D. Homa, B. Scott, G. Pickrell, A review of bioactive glasses: their structure, properties, fabrication and apatite formation, J. Biomed. Mater. Res., Part A 102 (1) (2014) 254–274.

[14] R. LeGeros, Calcium phosphate materials in restorative dentistry: a review, Adv. Dent. Res. 2 (1) (1988) 164–180.

[15] G. Pezzotti, E. Marin, T. Adachi, A. Rondinella, F. Boschetto, W. Zhu, N. Sugano, R.M. Bock, B. McEntire, S.B. Bal, Bioactive silicon nitride: a new therapeutic material for osteoarthropathy, Sci. Rep. 7 (2017) 44848.

[16] P. Schaaf, Laser Processing of Materials: Fundamentals, Applications and Developments, vol. 139, Springer Science & Business Media, 2010.

[17] H. Götz, M. Müller, A. Emmel, U. Holzwarth, R. Erben, R. Stangl, Effect of surface finish on the osseointegration of laser-treated titanium alloy implants, Biomaterials 25 (18) (2004) 4057–4064.

[18] L. D'alessio, R. Teghil, M. Zaccagnino, I. Zaccardo, D. Ferro, V. Marotta, Pulsed laser ablation and deposition of bioactive glass as coating material for biomedical applications, Appl. Surf. Sci. 138 (1999) 527–532.

[19] B. Nayak, M. Gupta, K. Kolasinski, Formation of nano-textured conical microstructures in titanium metal surface by femtosecond laser irradiation, Appl. Phys. A 90 (3) (2008) 399–402.

[20] J. Van der Stok, O.P. Van der Jagt, S. Amin Yavari, M.F. De Haas, J.H. Waarsing, H. Jahr, E.M. Van Lieshout, P. Patka, J.A. Verhaar, A.A. Zadpoor, et al., Selective laser melting-produced porous titanium scaffolds regenerate bone in critical size cortical bone defects, J. Orthop. Res. 31 (5) (2013) 792–799.

[21] B.S. Bal, W. Zhu, M. Zanocco, E. Marin, N. Sugano, B.J. McEntire, G. Pezzotti, Reconciling in vivo and in vitro kinetics of the polymorphic transformation in zirconia-toughened alumina for hip joints: I. Phenomenology, Mater. Sci. Eng. C 72 (2017) 252–258.

[22] R Core Team, R: A Language and Environment for Statistical Computing, R Foundation for Statistical Computing, Vienna, Austria, 2013, http://www.R-project.org/.

[23] X. Wang, S. Xu, S. Zhou, W. Xu, M. Leary, P. Choong, M. Qian, M. Brandt, Y.M. Xie, Topological design and additive manufacturing of porous metals for bone scaffolds and orthopaedic implants: a review, Biomaterials 83 (2016) 127–141.

[24] R.A. Perez, G. Mestres, Role of pore size and morphology in musculo-skeletal tissue regeneration, Mater. Sci. Eng. C 61 (2016) 922–939.

[25] Y.-T. Jian, Y. Yang, T. Tian, C. Stanford, X.-P. Zhang, K. Zhao, Effect of pore size and porosity on the biomechanical properties and cytocompatibility of porous NiTi alloys, PLoS ONE 10 (6) (2015) e0128138.

[26] S. Chen, Y. Guo, R. Liu, S. Wu, J. Fang, B. Huang, Z. Li, Z. Chen, Z. Chen, Tuning surface properties of bone biomaterials to manipulate osteoblastic cell adhesion and the signaling pathways for the enhancement of early osseointegration, Colloids Surf. B, Biointerfaces 164 (2018) 58–69.

[27] J. Collins, R. Gerby, New refractory uses for silicon nitride reported, JOM 7 (5) (1955) 612–615.

[28] G. Pezzotti, E. Marin, T. Adachi, F. Lerussi, A. Rondinella, F. Boschetto, W. Zhu, T. Kitajima, K. Inada, B.J. McEntire, et al., Incorporating Si_3N_4 into PEEK to produce antibacterial, osteocondutive, and radiolucent spinal implants, Macromol. Biosci. (2018) 1800033.

[29] M. Figueiredo, J. Gamelas, A. Martins, Characterization of bone and bone-based graft materials using FTIR spectroscopy, in: Infrared Spectroscopy-Life and Biomedical Sciences, InTech, 2012.

[30] E. Marin, T. Adachi, F. Boschetto, M. Zanocco, A. Rondinella, W. Zhu, R. Bock, B. McEntire, S.B. Bal, G. Pezzotti, Biological response of human osteosarcoma cells to Si_3N_4-doped bioglasses, Mater. Des. 159 (2018) 79–89.

[31] P. Sepulveda, J. Jones, L. Hench, In vitro dissolution of melt-derived 45S5 and sol–gel derived 58S bioactive glasses, J. Biomed. Mater. Res. 61 (2) (2002) 301–311.

[32] G. Pezzotti, L. Puppulin, A. La Rosa, M. Boffelli, W. Zhu, B.J. McEntire, S. Hosogi, T. Nakahari, Y. Marunaka, Effect of pH and monovalent cations on the Raman spectrum of water: basics revisited and application to measure concentration gradients at water/solid interface in Si_3N_4 biomaterial, Chem. Phys. 463 (2015) 120–136.

[33] X. Cui, W. Huang, Z. Yadong, C. Huang, Z. Yu, L. Wang, L. Wenlong, T. Wang, J. Zhou, H. Wang, N. Zhou, D. Wang, H. Pan, M.N. Rahaman, Evaluation of an injectable bioactive borate glass cement to heal bone defects in a rabbit femoral condyle model, Mater. Sci. Eng. C 73 (2017) 585–595.

[34] R.F. Kersten, S.M. van Gaalen, M.P. Arts, K.C. Roes, A. de Gast, T.P. Corbin, F.C. Öner, The SNAP trial: a double blind multi-center randomized controlled trial of a silicon nitride versus a PEEK cage in transforaminal lumbar interbody fusion in patients with symptomatic degenerative lumbar disc disorders: study protocol, BMC Musculoskelet. Disord. 15 (1) (2014) 57.

[35] M. Ishikawa, K.L. de Mesy Bentley, B.J. McEntire, B.S. Bal, E.M. Schwarz, C. Xie, Surface topography of silicon nitride affects antimicrobial and osseointegrative properties of tibial implants in a murine model, J. Biomed. Mater. Res., Part A 105 (12) (2017) 3413–3421.

[36] G. Pezzotti, B.J. McEntire, R. Bock, W. Zhu, F. Boschetto, A. Rondinella, E. Marin, Y. Marunaka, T. Adachi, T. Yamamoto, et al., In situ spectroscopic screening of osteosarcoma living cells on stoichiometry-modulated silicon nitride bioceramic surfaces, ACS Biomater. Sci. Eng. 2 (7) (2016) 1121–1134.

[37] B.S. Bal, R.M. Bock, A. Rondinella, E. Marin, W. Zhu, T. Adachi, B.J. McEntire, G. Pezzotti, Osteoinductive properties of silicon nitride, alumina, and titanium, ORS 2017 annual meeting proceedings, 0826.

[38] G. Pezzotti, R.M. Bock, B.J. McEntire, E. Jones, M. Boffelli, W. Zhu, G. Baggio, F. Boschetto, L. Puppulin, T. Adachi, et al., Silicon nitride bioceramics induce chemically driven lysis in porphyromonas gingivalis, Langmuir 32 (12) (2016) 3024–3035.

[39] I. Xynos, M. Hukkanen, J. Batten, L. Buttery, L. Hench, J. Polak, Bioglass® 45S5 stimulates osteoblast turnover and enhances bone formation in vitro: implications and applications for bone tissue engineering, Calcif. Tissue Int. 67 (4) (2000) 321–329.

[40] T. Kokubo, H. Takadama, How useful is SBF in predicting in vivo bone bioactivity?, Biomaterials 27 (15) (2006) 2907–2915.

[41] I.A. Silver, J. Deas, M. Erecińska, Interactions of bioactive glasses with osteoblasts in vitro: effects of 45S5 Bioglass®, and 58S and 77S bioactive glasses on metabolism, intracellular ion concentrations and cell viability, Biomaterials 22 (2) (2001) 175–185.

[42] T. Ibatan, M. Uddin, M. Chowdhury, Recent development on surface texturing in enhancing tribological performance of bearing sliders, Surf. Coat. Technol. 272 (2015) 102–120.

[43] R.H. Dauskarat, D.B. Marshall, R.O. Ritchie, Cyclic fatigue-crack propagation in magnesia-partially-stabilized zirconia ceramics, J. Am. Ceram. Soc. 73 (4) (1990) 893–903.

[44] M. Wakuda, Y. Yamauchi, S. Kanzaki, Y. Yasuda, Effect of surface texturing on friction reduction between ceramic and steel materials under lubricated sliding contact, Wear 254 (3–4) (2003) 356–363.

[45] P.V. Sander, J. Snyder, S.J. Gortler, H. Hoppe, Texture mapping progressive meshes, in: Proceedings of the 28th Annual Conference on Computer Graphics and Interactive Techniques, ACM, 2001, pp. 409–416.